

Tracking evaporative cooling of a mesoscopic atomic quantum gas in real time

Johannes Zeiher,^{1,*} Julian Wolf,^{1,2} Joshua A. Isaacs,^{1,2} Jonathan Kohler,^{1,†} and Dan M. Stamper-Kurn^{1,2,3}

¹*Department of Physics, University of California, Berkeley, CA 94720, USA*

²*Challenge Institute for Quantum Computation, University of California, Berkeley, CA 94720, USA*

³*Materials Science Department, Lawrence Berkeley National Laboratory, Berkeley, CA 94720, USA*

(Dated: 3rd September 2022)

The fluctuations in thermodynamic and transport properties in many-body systems gain in importance as the number of constituent particles is reduced. Ultracold atomic gases provide a clean setting for the study of mesoscopic systems; however, the detection of temporal fluctuations is hindered by the typically destructive detection, precluding repeated precise measurements on the same sample. Here, we overcome this limitation by utilizing the enhanced light–matter coupling in an optical cavity to perform a minimally invasive continuous measurement and track the time evolution of the atom number in a quasi two-dimensional atomic gas during evaporation from a tilted trapping potential. We demonstrate sufficient measurement precision to detect atom number fluctuations well below the level set by Poissonian statistics. Furthermore, two-time correlations of the atom number obtained from the real-time measurements shed light on the non-linearity of the evaporation process and the noise sources governing the transport of atoms out of the trapping volume. Our results establish coupled atom–cavity systems as a novel testbed for observing thermodynamics and transport phenomena in mesoscopic cold atomic gases and pave the way for cavity-assisted feedback stabilization of atom number and temperature of atomic quantum simulators.

I. INTRODUCTION

Tracking out-of-equilibrium dynamical processes and their fluctuations in mesoscopic systems is central to thermodynamics at intermediate scales [1, 2] and transport in solid state systems [3]. For example, current fluctuations in mesoscopic electronic devices reveal the charge quantization of elementary or emergent particles, shedding light on the underlying microscopic physics [4, 5]. Advanced experimental control and precise measurements make ultracold atomic gases an ideal testbed for studying transport phenomena with solid-state analogs and beyond [6–8]. Furthermore, the achievable system sizes, ranging from single to millions of atoms in different setups, naturally provide access to explore the mesoscopic domain with ensembles of cold atoms. However, solid-state and ultracold-atom mesoscopic systems differ in their fragility against measurement. Solid-state devices are coupled to large thermal reservoirs, which rapidly dissipate the backaction of measurement, and are refreshed with large particle reservoirs. In contrast, ultracold-atom systems are well isolated from thermal environments. Technical and backaction disturbance from measurement, such as optical force fluctuations caused by light scattering, is absorbed within the mesoscopic system itself and can change the properties of the system significantly. Thus, the measured fluctuations within a mesoscopic cold-atom system can be strongly altered by continuous or stroboscopic measurements performed on the system. Accessing real-time information

in such systems therefore requires strategies to maximize the extracted information for a given heating rate associated with the measurement.

The enhanced atom-light interaction in high-finesse optical cavities [9] provides a means for performing minimally invasive, extremely sensitive measurements on atomic gases. Demonstrations span from recording transient signals of single or few atoms passing through an optical cavity [10, 11] to measurements on static and dynamically evolving mesoscopic trapped atomic ensembles [12–17], or the probing of dynamical evolution of novel states of matter realized in the cavity [18–20]. Dispersive atom-number readout, with precision below atomic shot noise and sensitivity reaching down to the single-atom level in mesoscopic ensembles [13], makes cavity-aided measurements particularly interesting for non-invasive dynamical transport measurements in cold gases [21–23].

In this work, we employ cavity-aided measurements to observe the non-equilibrium process of evaporative cooling [24–28]. Evaporative cooling occurs in a gas of temperature T and atom number N when collisions drive atoms to energies above the finite trap depth U , whereupon they escape the trap, reducing the number of atoms remaining as well as their temperature. The ensuing dynamics depend on dimensionality, atom number, and temperature of the gas, all features also at the heart of transport phenomena studied with destructive measurements [21]. A simple model captures the interplay between temperature and atom number in an evaporatively cooled atomic ensemble [26]: To evaporate from the trap, atoms have to be collisionally transferred to the high-energy tail of the Maxwell–Boltzmann distribution, such that the average evaporation rate $\dot{N} \propto -\eta e^{-\eta}$, depends exponentially on $\eta = U/k_B T$. This implies that samples with initially higher temperature evaporate

* johannes.zeiher@mpq.mpg.de; Present address: Max-Planck-Institut für Quantenoptik, 85748 Garching, Germany

† Present address: Vector Atomic, Inc., Pleasanton, CA 94586, USA

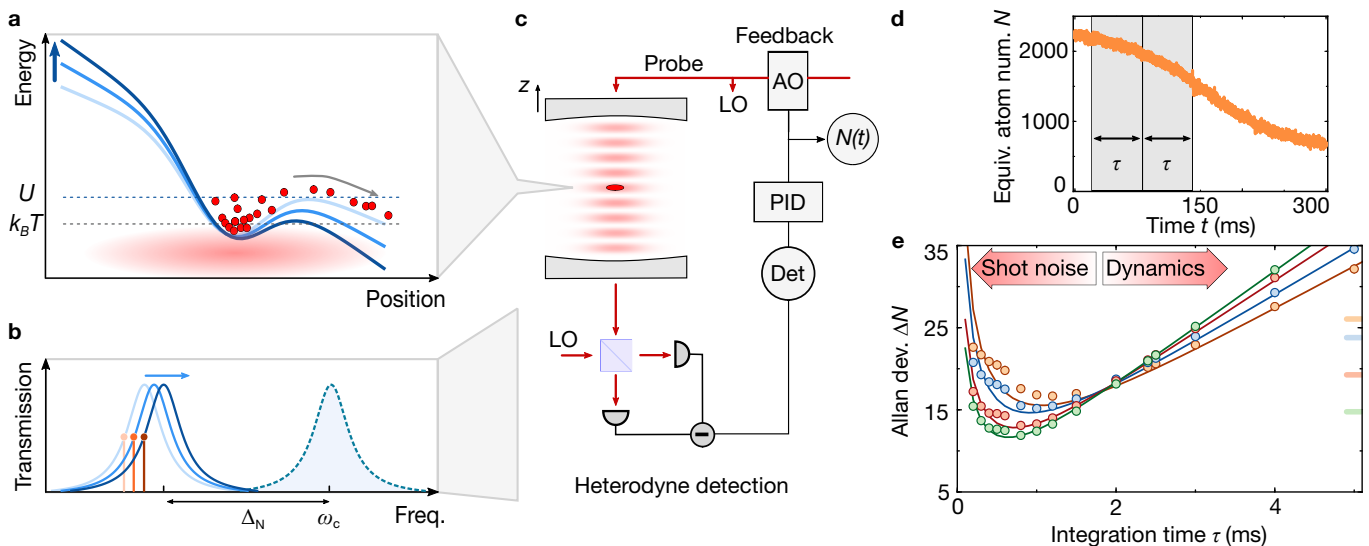


Figure 1. **Experimental setup and measurement imprecision.** **a** Schematic of the tilted evaporation of atoms (red) with temperature T in the trap potential (blue) with dynamically lowered depth U . Atoms with energies exceeding the trap depth are spilled. **b** The atoms dispersively couple to the cavity, resulting in an atom-number-dependent shift Δ_N of the transmission line shape (blue solid traces) compared to an empty cavity (blue dashed line). Tracking the side of fringe (marked by red dot and line) provides a dynamical measurement of atom number. **c** The cavity resonance is tracked using a feedback loop involving the cavity-coupled atomic cloud (dark red), located at the intensity maximum of a probe beam in the cavity (light red). The transmitted intensity of probe light is detected using a heterodyne receiver with local oscillator (LO) and a radiofrequency power detector (Det). This power is kept constant using a feedback loop (PID) adjusting the frequency of probe and LO through an acousto optic modulator (AO). The atom number is derived from an in-loop measurement of the voltage used to adjust a voltage controlled oscillator driving the AO. **d** A single unfiltered trace of equivalent atom number N vs. time with the filter procedure indicated (gray shaded areas). **e** The Allan deviation is dominated by photonic shot noise for small integration times τ and by dynamics of the atom number for large τ . A low pass filter of the traces with optimal integration time $\tilde{\tau}$ minimizes the noise associated with both effects. The solid lines represent guides to the eye. Larger photon number n (orange: $n = 1.9(1)$, blue: $n = 3.2(1)$, red: $n = 6.0(1)$ and green: $n = 9.7(1)$) results in reduced shot noise, but also faster loss of the atoms and therefore increased imprecision at longer integration times. The colored ticks on the right mark the noise level set by Poissonian statistics for our lowest measured mean atom number for each n .

atoms more quickly than samples with lower temperature. Moreover, due to the density-dependent thermalization rate of an evaporatively cooled gas [25, 26] and the presence of three-body collisions [29], the evaporation dynamics can be expected to be non-linear in atom number. The stochastic character of collisions and atom loss enriches this setting through the addition of fluctuations and calls for an in-depth study of the characteristic mesoscopic features of evaporative cooling.

Here, we observe the non-equilibrium dynamics of an ultracold quantum gas during forced evaporation in a tilted trap potential by collecting real-time traces of the atom number dynamics (see Fig. 1a). We utilize the enhanced optical cross section of atoms coupled to a single mode of a high-finesse optical cavity to perform minimally invasive high-precision atom number measurements. In particular, we reveal the interplay of atom number and temperature and their fluctuations during evaporative cooling via two-time correlations of the continuous atom number record. Such two-time correlations also enable us to shed light on the stochastic fluctuations inherent in the evaporative cooling process itself, and discriminate them

from fluctuations from one atomic ensemble to another.

II. DISPERSIVE ATOM NUMBER READOUT

The principle of dynamical dispersive atom number readout of our atomic cloud is illustrated in Fig. 1b and c. We consider a cloud of atoms that is well localized at the intensity maximum of the standing wave formed by a probe beam coupled into the TEM_{00} mode of a Fabry–Perot optical cavity. The cavity resonance is at a frequency ω_c in absence of atoms, which are coupled to the cavity with a single-atom vacuum Rabi coupling g on an optical transition with frequency ω_a , linewidth Γ and atom-cavity detuning $\Delta_{ca} = \omega_c - \omega_a$. In the dispersive limit $|\Delta_{ca}| \gg \sqrt{N}g \gg \Gamma$, the presence of N atoms causes a frequency shift of the light-like mode of the coupled atom-cavity system by an amount proportional to the atom number [12–14],

$$\Delta_N = N \frac{g^2}{\Delta_{ca}}. \quad (1)$$

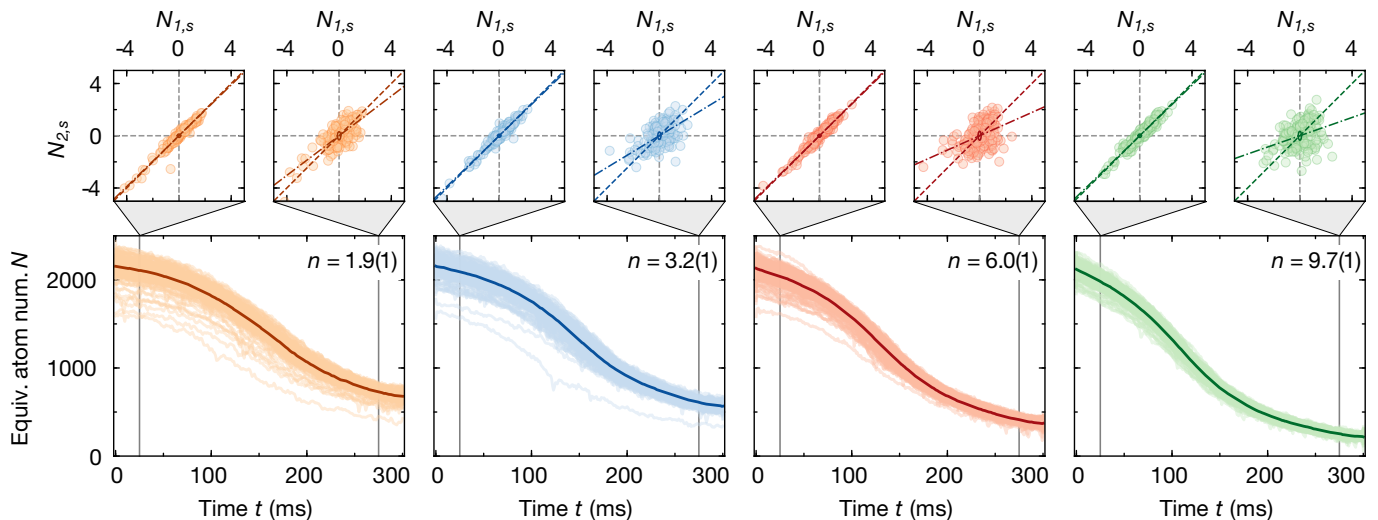


Figure 2. **Two-time correlations of atom numbers from real-time trajectories.** **a** Traces of equivalent atom number N vs. observation time t , calculated from the number-dependent cavity shift, for varying intracavity photon number n (indicated in the upper right corner). The bright curves represent individual runs of the experiment (approximately 150 per panel). The dark curves are the mean over all such traces. The traces were filtered using their corresponding optimal integration time, see Fig. 1e. The vertical lines mark the two times $t_2 = 25$ ms ($t_2 = 275$ ms) used to produce the scatter plots shown above the time traces. They illustrate the standardized atom number $N_{2,s}$ measured at the earlier (later) t_2 vs. $N_{1,s}$ measured at $t_1 = 5$ ms. The diagonal (dashed line) and the slope extracted from a linear ordinary least squares fit to the data (dash-dotted line) are indicated in all scatter plots. The corresponding measurement noise is indicated by the ellipse in the center.

We detect this dispersive shift by feedback-stabilizing the frequency of the weak cavity probe to the side of fringe of the cavity transmission, realizing a continuous quantum non-demolition measurement of atom number [14]. During the measurement, the probe power in the cavity is held constant at a level characterized by the intracavity photon number $n = P/(2\hbar\omega_c\kappa)$, where κ denotes the cavity half linewidth and P is the power transmitted through the cavity. The frequency shift of the cavity resonance is extracted through the feedback signal, see Fig. 1b and Fig. 5. We use knowledge of g [12, 16, 30] and Δ_{ca} to estimate the instantaneous “equivalent atom number” $N(t) = \Delta_{N(t)}/\Delta_1$, see Fig. 1d, where “equivalent” reflects a slight reduction of the vacuum Rabi coupling in our experiment, see Appendix A, and is implied if not stated explicitly otherwise.

We monitor the evolution of the intracavity gas during evaporation dynamics initiated by an applied magnetic field gradient, see Fig. 1a. We quantify the imprecision in the real-time measurement for different integration times by the “Allan deviation” $\Delta N(\tau) = ((N_\tau(t_{i+1}) - N_\tau(t_i))^2)^{1/2}$. Here, the trace $N_\tau(t_i)$ is obtained by low-pass filtering the full trace $N(t)$ with an integration time τ and then resampling at discrete times t_i separated by time intervals of length τ . The angle brackets denote the average over all i [12, 13]. Photon shot noise limits the measurement precision of the dispersive cavity shift for short integration times, see Fig. 1e. For integration times above approximately 1 ms, the dynamics of the evaporation process start dominating the Allan deviation. Choosing such a long integration time

leads to a loss of information about the dynamical system under observation. As a consequence, the dynamics set an upper bound on the achievable integration times and therefore suppression of photonic shot noise in the measurement, see Appendix D. Despite this, the minimal imprecision and therefore the measurement noise of our cavity-assisted detection is well below the level set by Poissonian fluctuations of size \sqrt{N} for N atoms for all measured traces and all times presented in the following, see Fig. 1e.

We started our experiment with an atomic cloud of about 2200 ^{87}Rb atoms with a mean temperature of approximately $T_0 = 2.6 \mu\text{K}$. The gas was prepared in its hyperfine state $|F, m_F\rangle = |2, 2\rangle$ and was trapped predominantly in a single well of a far-detuned optical lattice potential with an initial depth $U_0/k_B = 31(1) \mu\text{K}$ in an optical cavity [16, 30, 31]. The lattice provided strong confinement in the z -direction with a trapping frequency of $\omega_z/2\pi = 91(2) \text{kHz}$, putting the gas in the quasi two-dimensional regime $\hbar\omega_z > k_B T_0$. The magnetic field control provided by an atom chip allowed us to compress the atomic cloud in the axial z -direction before loading into the optical cavity. This enabled the accurate positioning of the atomic cloud along the cavity axis at the peak of the probe standing wave, where the atom-cavity coupling was maximized, nearly identical for all atoms, and optomechanical backaction heating was minimal [31, 32]. The cavity length was stabilized such that its resonance frequency was kept at a near-constant red detuning $\Delta_{ca}/2\pi \approx -42 \text{GHz}$ with respect to the $D2$ line of ^{87}Rb , for which the atomic res-

onance linewidth is $\Gamma/2\pi \approx 6$ MHz. The detuning of the cavity probe from atomic resonance together with the vacuum Rabi coupling $g/2\pi = 13.1$ MHz led to a maximal cavity shift $|\Delta_1/2\pi| \approx 4$ kHz per atom. The cavity probe was maintained at a constant detuning of $\delta_{pc}/2\pi = \kappa/2\pi = 1.8$ MHz from the atom-shifted cavity resonance frequency. The frequency lock of the probe to the cavity was realized by stabilizing the radiofrequency power output from a heterodyne receiver monitoring the probe transmission through the cavity, see Fig. 1c and Appendix A. The large single-atom cooperativity $C = g^2/\kappa\Gamma = 15.9$ and consequently low cavity probe powers of few picowatts in our experiment allowed us to keep the probe-induced off-resonant scattering, and associated heating rate, at a minimal level.

In a first set of experiments, we tracked the equivalent atom number for different intracavity photon numbers n , while slowly lowering the trap potential U/k_B from $31 \mu\text{K}$ to approximately $8 \mu\text{K}$ by ramping up a magnetic field gradient within 330 ms, see Fig. 6 and Appendix A. The resulting ensemble of traces is shown in Fig. 2, with every individual trace representing a new run of the experiment. The traces taken together form a statistical ensemble that encompasses both the variation in evaporation trajectories with different initial atom number and temperature, and also the fluctuations in atom number generated by evaporation dynamics in individual trajectories. In order to minimize the effect of noise, each trace was filtered with a bandwidth corresponding to the optimal integration time $\tilde{\tau}$ extracted from the Allan deviation shown in Fig. 1c. For clarity we suppress the subscript and write $N(t) \equiv N_{\tilde{\tau}}(t)$ in the following. Our measurements of $N(t)$ show a clear trend to lower final atom numbers as the intracavity photon number is increased. This trend reflects the larger measurement-induced heating at increasing probe power, which leads to an increase in the number of atoms ejected from the trap during evaporation.

In general, decorrelation of two measured atom numbers $N(t_1) \equiv N_1$ and $N(t_2) \equiv N_2$ at two points in time, indicated by t_1 and t_2 , arises from three sources: technical noise, measurement noise and stochastic noise due to the evaporation process itself. In our experiment, we observe dominant linear correlations of around 97% at all intracavity photon numbers for two measurements closely spaced in time, see Fig. 2 upper panel. We extract the correlations from the slope of the standardized atom numbers $N_{2,s}$ vs. $N_{1,s}$, which equals the Pearson correlation coefficient ρ_{12} , see Appendix C. The standardized atom numbers are defined as $N_{1(2),s} = (N_{1(2)} - \langle N_{1(2)} \rangle) / \sigma_{1(2)}$, where $\langle N_1 \rangle$ ($\langle N_2 \rangle$) and σ_1 (σ_2) are the mean and the standard deviation of the non-standardized atom number distribution measured at time t_1 (t_2). The strong observed correlation indicates a small influence of all noise sources at these early times. In particular, it confirms that our measurement noise is small, consistent with our previous analysis of the imprecision. For a time $t_2 = 275$ ms, later on the evaporation trajectory, the

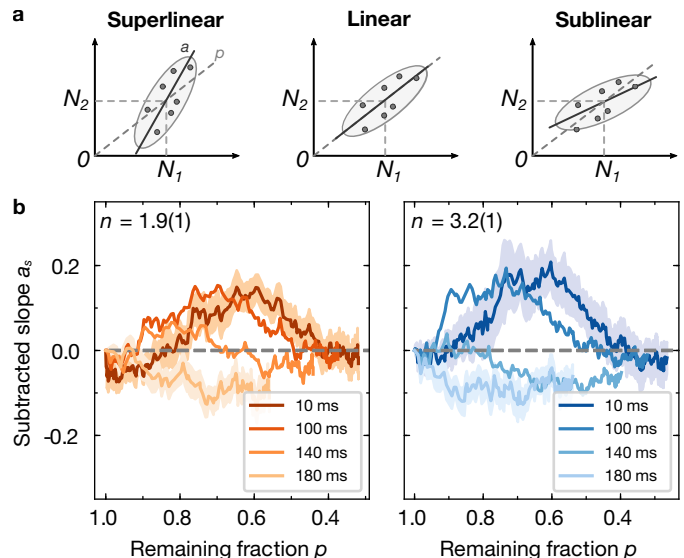


Figure 3. **Non-linearity of evaporation process.** **a** Schematic illustrating the non-linearity measure. Super-(sub-) linearity is equivalent to a larger (smaller) slope a of the scatter of N_2 vs. N_1 than the remaining fraction of atoms p . For a linear process, $a = p$. **b** Subtracted slope $a_s = a - p$ for different initial times t_1 (dark to bright color, indicated in legend) used to quantify the non-linearity of the evaporation process vs. remaining fraction of atoms p . The shaded region shows the standard deviation calculated by bootstrapping for the smallest and largest initial time.

fluctuations are much more prominent. However, there is still some degree of linear correlation present. The reduction of the correlation from 75.9(1)% at the smallest intracavity photon number $n = 1.9(1)$ to 35.0(1)% at the largest intracavity photon number $n = 9.7(1)$ indicates a larger impact of stochastic noise coupled into the system at larger lost fraction of atoms.

III. NON-LINEARITY OF EVAPORATION

The non-linear dynamics of a system are captured already by the evolution of statistical averages. In the following, we outline how a continuous measurement of the atom number of the same cloud enables us to shed light on the non-linear character of evaporative cooling by analyzing two-time correlations. To this end, we compare the remaining fraction of atoms, $p = \langle N_2 \rangle / \langle N_1 \rangle$, to the slope extracted from scatter plots such as those shown in Fig. 2, calculated as the least squares estimate $a = \rho_{12} \sigma_2 / \sigma_1$. Here, the (two-time) correlation coefficient is given as $\rho_{12} = \text{cov}(N_1, N_2) / \sigma_1 \sigma_2$. For a linear process, defined by a constant evaporation rate and $\dot{N} \propto -N$, the two predictions should coincide and hence $a = p$, whereas non-linear effects lead to a deviation from this expectation, see Fig. 3a and Appendix C. As an example, the case $\dot{N} \propto -N^\alpha$ with $\alpha > 1$ leads to $a < p$, which we term “sublinear” to indicate a scatter slope

smaller than in the linear case.

For our evaporation sequence, we find systematic deviations from a simple linear relationship, see Fig. 3b. Recording the difference $a_s = a - p$ versus the remaining fraction of atoms p , we observe a pronounced superlinear behavior with $a > p$ referencing to a small initial time t_1 . We interpret this as a manifestation of initial temperature variations of our cloud arising from our sample preparation, which is backed by simulations of the evaporation process, see Fig. 7 and Appendix B. The dynamics of evaporative cooling are governed by an interplay between a reduction of atom number and temperature of a gas, and the latter can have a moderating or accelerating effect on the former. Our observation can be understood as an effective non-linearity in atom number as a result of the temperature of the gas, which is hidden in an atom number measurement at a single time, but reveals itself in our two-time correlation measurements. Initially hotter clouds will start with slightly fewer atoms due to atom loss before we start our real-time measurement, resulting in an initial anti-correlation between atom number and temperature. The further evaporation process is less efficient in hotter clouds, which therefore spill more atoms than initially colder clouds, leading to $a > p$. The rapid evaporation of hotter gases also quickly reduces their temperature, such that over time different realizations of the gas arrive at nearly the same final temperature irrespective of their initial temperature. This interesting transient behavior is often implicitly assumed in literature quoting that the temperature locks to a fixed fraction $1/\eta$ of the trap depth [25, 26, 28] and ultimately originates from the competition between exponential truncation and temperature-dependent thermalization of atoms in the evaporation process.

At later times in the evaporation process, after the effect of initial temperature fluctuations is suppressed, we find slightly sublinear behavior, where an initial excess of atoms at time t_1 is reduced during the evolution. This behavior can be explained by increased three-body losses towards the end of the evaporation ramp, which reduce ensemble fluctuations due to their non-linear character [29], see Fig. 7. Interestingly, our observations imply that evaporation first moderates temperature fluctuations and then, thereafter, atom number fluctuations in different realizations, ultimately resulting in a stabilizing effect for both atom number and temperature.

IV. STOCHASTIC CHARACTER OF EVAPORATION

The mesoscopic nature of our samples together with the high measurement precision enable us to characterize also the fluctuations inherent in evaporative cooling. In addition to measurement and technical noise, fluctuations in the initially prepared ensemble can easily mask such stochastic fluctuations. Initial atom number fluctuations can become significant especially in the mesoscopic

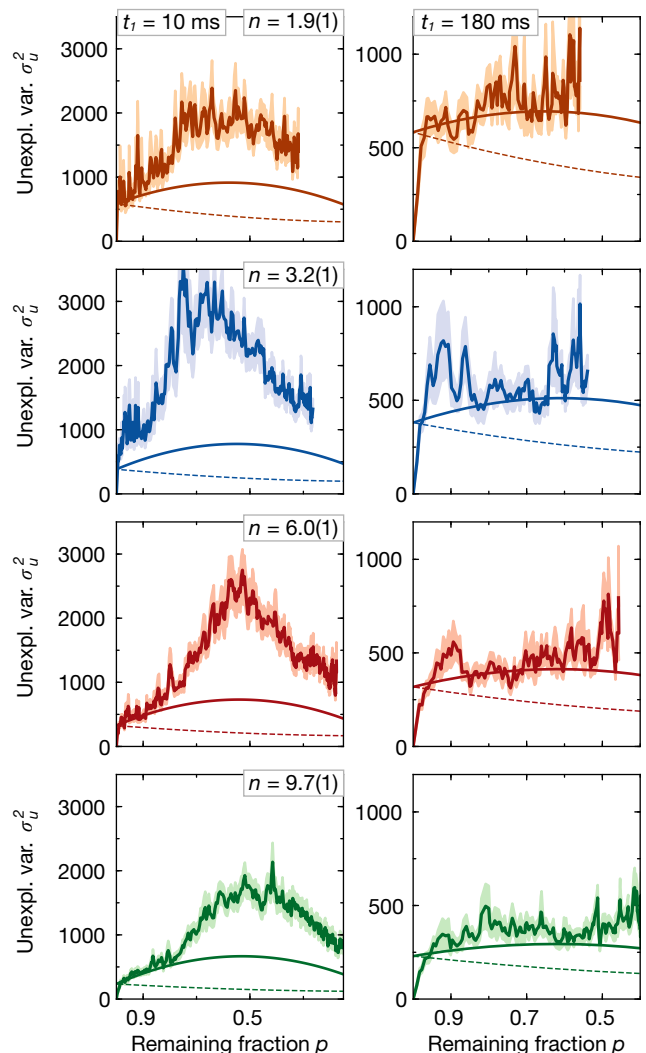


Figure 4. **Stochastic fluctuations of the evaporation process.** The unexplained variance vs. remaining fraction of atoms p for different intracavity photon numbers (color code as in Figs. 2 and 3) and two different times t_1 indicated in the top left corner, with the standard deviation calculated by bootstrapping indicated by the shaded region. The solid lines show the model prediction including Poissonian stochastic noise, measurement noise and residual initial ensemble fluctuations, the dashed lines show the prediction without the contribution of Poissonian stochastic noise.

regime, reaching up to a point where they can also limit the achievable measurement sensitivity for the study of transport phenomena [21].

Minimally invasive atom number measurements allow for suppressing the effect of fluctuations in the prepared ensemble, and therefore provide a means for an in-depth study of the stochastic properties of evaporative cooling. Concretely, we calculate the unexplained variance $\sigma_u^2 = \sigma_2^2 (1 - \rho_{12}^2)$ as the amount of variance in atom number measured at time t_2 that is not explained by correlations with the atom number measured at time t_1 . For our evaporation sequence, the unexplained variance

exhibits a clear peak when referencing to an early measurement at time $t_1 = 10$ ms, see Fig. 4, left column. Comparing with a simple parameter-free theoretical model, see Appendix C, we find that the fluctuations are up to a factor of three above the fluctuations expected for a purely uncorrelated atom loss, which is described by a Poissonian stochastic process and a spilling rate constant in time. We attribute these large atom number fluctuations to additional initial temperature fluctuations beyond those anti-correlated with the initial atom number, which are then converted into large final atom number fluctuations. The large temperature-induced fluctuations are suppressed strongly during the further evaporation process with decreasing remaining fraction p (later t_2). Evaluating the unexplained variance starting at a later initial time $t_1 = 180$ ms, we find that for large remaining fraction of atoms (t_2 close to t_1), the unexplained variance is consistent with that expected from the known measurement noise in N_1 and N_2 , see Fig. 4, right column. For smaller remaining fraction, other noise sources become dominant, with the increase in σ_u above the measurement noise limit, i.e. the sum of process noise and technical noise, being consistent with the noise expected for a linear, Poissonian stochastic loss process.

V. CONCLUSION

The minimally invasive measurement of atom number dynamics in our cavity-coupled atomic gas provides an ideal starting point for further studies of low-dimensional

mesoscopic quantum gases. The densities reached in our two-dimensional system are close to the regime where corrections due to Bose statistics and interactions in the gas become relevant. This calls for further studies focusing on how evaporation dynamics and stochastic fluctuations as well as transport are modified by quantum statistics and atomic interactions, complementing recent studies in three-dimensional gases [33, 34]. Furthermore, our experiments pave the way for future non-invasive two-terminal transport measurements of strongly correlated quantum gases in optical cavities [22], for dynamical probing of fluctuation dissipation relations [35, 36], or for realizing novel non-destructive local probes of cold gases [23]. Finally, our results indicate that feedback on the atom number [37, 38] based on the non-destructive real-time record of an evaporating gas can prepare a samples at a fixed temperature with controllable atom numbers fluctuating less than the amount set by Poissonian statistics. This provides an ideal starting condition to study atom-number-dependent collective phenomena in optical cavities such as dynamical instabilities [30].

ACKNOWLEDGMENTS

We thank M. Knap, A. Schuckert, J. Moore, A. Avdoshkin and T. Xu for discussions and A. Rubio-Abadal for comments on the manuscript. J.Z. thanks the Humboldt Foundation for the support through a Feodor Lynen fellowship.

-
- [1] M. Campisi, P. Hänggi, and P. Talkner, “*colloquium: quantum fluctuation relations: foundations and applications*,” Rev. Mod. Phys. **83**, 771–791 (2011).
 - [2] M. Campisi, P. Talkner, and P. Hänggi, “*Fluctuation Theorems for Continuously Monitored Quantum Fluxes*,” Phys. Rev. Lett. **105**, 140601 (2010).
 - [3] Y. M. Blanter and M. Büttiker, “*Shot Noise in Mesoscopic Conductors*,” Physics Reports **336**, 1–166 (2000).
 - [4] W. Schottky, “*Über Spontane Stromschwankungen in Verschiedenen Elektrizitätsleitern*,” Ann. Phys. **362**, 541–567 (1918).
 - [5] S. Gustavsson, R. Leturcq, B. Simović, R. Schleser, T. Ihn, P. Studerus, K. Ensslin, D. C. Driscoll, and A. C. Gossard, “*Counting Statistics of Single Electron Transport in a Quantum Dot*,” Phys. Rev. Lett. **96**, 076605 (2006).
 - [6] J.-P. Brantut, J. Meineke, D. Stadler, S. Krinner, and T. Esslinger, “*Conduction of Ultracold Fermions Through a Mesoscopic Channel*,” Science **337**, 1069–1071 (2012).
 - [7] J.-P. Brantut, C. Grenier, J. Meineke, D. Stadler, S. Krinner, C. Kollath, T. Esslinger, and A. Georges, “*A Thermoelectric Heat Engine with Ultracold Atoms*,” Science **342**, 713–715 (2013).
 - [8] C.-C. Chien, S. Peotta, and M. Di Ventra, “*Quantum Transport in Ultracold Atoms*,” Nat. Phys. **11**, 998–1004 (2015).
 - [9] H. Tanji-Suzuki, I. D. Leroux, M. H. Schleier-Smith, M. Cetina, A. T. Grier, J. Simon, and V. Vuletić, “*Chapter 4 - Interaction between Atomic Ensembles and Optical Resonators: Classical Description*,” Advances In Atomic, Molecular, and Optical Physics **60**, 201–237 (2011).
 - [10] C. J. Hood, T. W. Lynn, A. C. Doherty, A. S. Parkins, and H. J. Kimble, “*The Atom-Cavity Microscope: Single Atoms Bound in Orbit by Single Photons*,” Science **287**, 1447–1453 (2000).
 - [11] P. W. H. Pinkse, T. Fischer, P. Maunz, and G. Rempe, “*Trapping an Atom with Single Photons*,” Nature **404**, 365–368 (2000).
 - [12] N. Brahms, T. P. Purdy, D. W. C. Brooks, T. Botter, and D. M. Stamper-Kurn, “*Cavity-Aided Magnetic Resonance Microscopy of Atomic Transport in Optical Lattices*,” Nat. Phys. **7**, 604–607 (2011).
 - [13] H. Zhang, R. McConnell, S. Čuk, Q. Lin, M. H. Schleier-Smith, I. D. Leroux, and V. Vuletić, “*Collective State Measurement of Mesoscopic Ensembles with Single-Atom Resolution*,” Phys. Rev. Lett. **109**, 133603 (2012).
 - [14] Z. Chen, J. G. Bohnet, J. M. Weiner, K. C. Cox, and J. K. Thompson, “*Cavity-Aided Nondemolition Measurements for Atom Counting and Spin Squeezing*,” Phys.

- Rev. A **89**, 043837 (2014).
- [15] M. A. Norcia and J. K. Thompson, “*Strong Coupling on a Forbidden Transition in Strontium and Nondestructive Atom Counting*,” Phys. Rev. A **93**, 023804 (2016).
- [16] J. Kohler, N. Spethmann, S. Schreppler, and D. M. Stamper-Kurn, “*Cavity-Assisted Measurement and Coherent Control of Collective Atomic Spin Oscillators*,” Phys. Rev. Lett. **118**, 063604 (2017).
- [17] K. Roux, V. Helsen, H. Konishi, and J.-P. Brantut, “*Cavity-Assisted Preparation and Detection of a Unitary Fermi Gas*,” arXiv:2010.08409 (2020).
- [18] J. Léonard, A. Morales, P. Zupancic, T. Esslinger, and T. Donner, “*Supersolid Formation in a Quantum Gas Breaking a Continuous Translational Symmetry*,” Nature **543**, 87–90 (2017).
- [19] J. Léonard, A. Morales, P. Zupancic, T. Donner, and T. Esslinger, “*Monitoring and Manipulating Higgs and Goldstone Modes in a Supersolid Quantum Gas*,” Science **358**, 1415–1418 (2017).
- [20] R. M. Kroeze, Y. Guo, and B. L. Lev, “*Dynamical Spin-Orbit Coupling of a Quantum Gas*,” Phys. Rev. Lett. **123**, 160404 (2019).
- [21] S. Krinner, T. Esslinger, and J.-P. Brantut, “*Two-Terminal Transport Measurements with Cold Atoms*,” J. Phys.: Condens. Matter **29**, 343003 (2017).
- [22] S. Uchino, M. Ueda, and J.-P. Brantut, “*Universal Noise in Continuous Transport Measurements of Interacting Fermions*,” Phys. Rev. A **98**, 063619 (2018).
- [23] D. Yang, C. Laflamme, D. V. Vasilyev, M. A. Baranov, and P. Zoller, “*Theory of a Quantum Scanning Microscope for Cold Atoms*,” Phys. Rev. Lett. **120**, 133601 (2018).
- [24] K. B. Davis, M. O. Mewes, and W. Ketterle, “*An Analytical Model for Evaporative Cooling of Atoms*,” Appl. Phys. B **60**, 155–159 (1995).
- [25] O. J. Luiten, M. W. Reynolds, and J. T. M. Walraven, “*Kinetic Theory of the Evaporative Cooling of a Trapped Gas*,” Phys. Rev. A **53**, 381–389 (1996).
- [26] W. Ketterle and N. J. V. Druten, “*Evaporative Cooling of Trapped Atoms*,” Advances In Atomic, Molecular, and Optical Physics **37**, 181–236 (1996).
- [27] H. Wu and C. J. Foot, “*Direct Simulation of Evaporative Cooling*,” J. Phys. B: At. Mol. Opt. Phys. **29**, L321–L328 (1996).
- [28] K. M. O’Hara, M. E. Gehm, S. R. Granade, and J. E. Thomas, “*Scaling Laws for Evaporative Cooling in Time-Dependent Optical Traps*,” Phys. Rev. A **64**, 051403(R) (2001).
- [29] S. Whitlock, C. F. Ockeloen, and R. J. C. Spreeuw, “*Sub-Poissonian Atom-Number Fluctuations by Three-Body Loss in Mesoscopic Ensembles*,” Phys. Rev. Lett. **104**, 120402 (2010).
- [30] J. Kohler, J. A. Gerber, E. Dowd, and D. M. Stamper-Kurn, “*Negative-Mass Instability of the Spin and Motion of an Atomic Gas Driven by Optical Cavity Backaction*,” Phys. Rev. Lett. **120**, 013601 (2018).
- [31] T. P. Purdy, D. W. C. Brooks, T. Botter, N. Brahms, Z.-Y. Ma, and D. M. Stamper-Kurn, “*Tunable Cavity Optomechanics with Ultracold Atoms*,” Phys. Rev. Lett. **105**, 133602 (2010).
- [32] N. Brahms, T. Botter, S. Schreppler, D. W. C. Brooks, and D. M. Stamper-Kurn, “*Optical Detection of the Quantization of Collective Atomic Motion*,” Phys. Rev. Lett. **108**, 133601 (2012).
- [33] M. A. Kristensen, M. B. Christensen, M. Gajdacz, M. Iglicki, K. Pawłowski, C. Klempt, J. F. Sherson, K. Rzażewski, A. J. Hilliard, and J. J. Arlt, “*Observation of Atom Number Fluctuations in a Bose-Einstein Condensate*,” Phys. Rev. Lett. **122**, 163601 (2019).
- [34] M. B. Christensen, T. Vibel, A. J. Hilliard, M. B. Kruk, K. Pawłowski, D. Hryniuk, K. Rzażewski, M. A. Kristensen, and J. J. Arlt, “*Observation of Microcanonical Atom Number Fluctuations in a Bose-Einstein Condensate*,” arXiv:2011.08736 (2020).
- [35] D. Yang, A. Grankin, L. M. Sieberer, D. V. Vasilyev, and P. Zoller, “*Quantum Non-Demolition Measurement of a Many-Body Hamiltonian*,” Nat. Commun. **11**, 775 (2020).
- [36] A. Schuckert and M. Knap, “*Probing Eigenstate Thermalization with the Emergence of Fluctuation-Dissipation Relations in Quantum Simulators*,” arXiv:2007.10347 (2020).
- [37] M. Gajdacz, P. L. Pedersen, T. Mørch, A. J. Hilliard, J. Arlt, and J. F. Sherson, “*Non-Destructive Faraday Imaging of Dynamically Controlled Ultracold Atoms*,” Review of Scientific Instruments **84**, 083105 (2013).
- [38] M. Gajdacz, A. J. Hilliard, M. A. Kristensen, P. L. Pedersen, C. Klempt, J. J. Arlt, and J. F. Sherson, “*Preparation of Ultracold Atom Clouds at the Shot Noise Level*,” Phys. Rev. Lett. **117**, 073604 (2016).
- [39] J. Söding, D. Guéry-Odelin, P. Desbiolles, F. Chevy, H. Inamori, and J. Dalibard, “*Three-Body Decay of a Rubidium Bose-Einstein Condensate*,” Appl Phys B **69**, 257–261 (1999).
- [40] T. Weber, J. Herbig, M. Mark, H.-C. Nägerl, and R. Grimm, “*Three-Body Recombination at Large Scattering Lengths in an Ultracold Atomic Gas*,” Phys. Rev. Lett. **91**, 123201 (2003).
- [41] C.-L. Hung, X. Zhang, N. Gemelke, and C. Chin, “*Accelerating Evaporative Cooling of Atoms into Bose-Einstein Condensation in Optical Traps*,” Phys. Rev. A **78**, 011604(R) (2008).
- [42] J. E. Lye, J. J. Hope, and J. D. Close, “*Nondestructive Dynamic Detectors for Bose-Einstein Condensates*,” Phys. Rev. A **67**, 043609 (2003).
- [43] D. B. Hume, I. Stroescu, M. Joos, W. Muessel, H. Strobel, and M. K. Oberthaler, “*Accurate Atom Counting in Mesoscopic Ensembles*,” Phys. Rev. Lett. **111**, 253001 (2013).

APPENDIX A: METHODS

Experimental sequence

We started our measurement by preparing a cloud of about 2200 ^{87}Rb atoms with a temperature of approximately $2.6\ \mu\text{K}$ in a cavity-supported vertical optical standing wave, forming an optical lattice with lattice spacing $a = 421\ \text{nm}$. Before loading the lattice, the cloud was compressed vertically in a tight magnetic trap created by an atom chip, such that predominantly a single slice of the lattice is populated [16, 30, 31]. We estimate the fraction of atoms in other slices to be maximally 20%, as was characterized by cavity-aided magnetic resonance microscopy [12]. The depth of the lattice trap was $U_0/2\pi = h \times 641(30)\ \text{kHz}$ ($k_B \times 31(1)\ \mu\text{K}$) and the waist of the lattice beam in the cavity was $w_0 = 26\ \mu\text{m}$, leading to axial and radial trapping frequencies of $\omega_z/2\pi = 91(2)\ \text{kHz}$ and $\omega_r/2\pi = 670(10)\ \text{Hz}$. These parameters put the gas in a quasi two-dimensional regime, where motion along the z -direction is frozen out, but atomic collisions are still described by a three-dimensional scattering process. The cavity length and exact wavelength of the lattice laser were chosen such that the atomic cloud axially overlapped with the maximal probe intensity in the cavity. The atoms emerged from the magnetic trap purely in the $|F, m_F\rangle = |2, 2\rangle$ hyperfine state. During probing, we applied a strong magnetic field of $B_z = 17\ \text{G}$ along the cavity axis, and also drove the cavity with σ^+ circularly polarized probe light. Under these conditions, the light-atom interactions are reduced to an effective two-level scheme, the atomic spin polarization is preserved, and the vacuum Rabi coupling is maximized. The atom number was recorded using a cavity probe at a wavelength of $780\ \text{nm}$, detuned by $\Delta_{ca}/2\pi \approx -42\ \text{GHz}$ to the red of the $D2$ line. The transmission of this probe through the cavity was recorded on a heterodyne receiver. For heterodyne detection, we used a local oscillator (LO) with approximately $1\ \text{mW}$ of optical power derived from the same laser but with its frequency offset by $10\ \text{MHz}$ relative to the frequency of the probe. The probe beam was intensity stabilized before entering the cavity and the LO before coupling into the heterodyne receiver. The photon collection efficiency was reduced by cavity mirror losses ($\epsilon_c = 0.31$), finite path efficiency of the heterodyne path ($\epsilon_p = 0.93$), mode matching efficiency of local oscillator and probe beam ($\epsilon_{mm} = 0.89$) and quantum efficiency of the heterodyne photodetector ($\epsilon_q \approx 0.58$). These effects combined to give an overall photon detection efficiency of $\epsilon = 0.149(10)$ in our heterodyne receiver.

After preparation of the cloud, forced evaporation was induced by exponentially ramping up the current through our atomic chip wires with a time constant of $70\ \text{ms}$. The resulting inhomogeneous magnetic field was accompanied by a magnetic field gradient increasing from zero up to $220\ \text{G/cm}$, strong enough to lower the trap depth dynamically, see Fig. 6. During the evaporation process, an analog side-of-fringe feedback loop was engaged to keep the

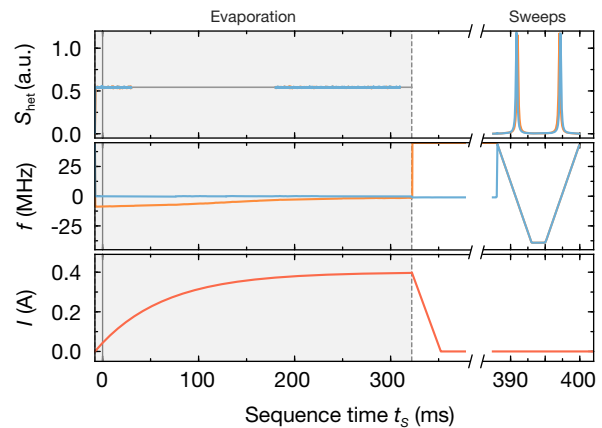


Figure 5. **Experimental sequence.** Upper panel: Heterodyne magnitude S_{het} with atoms present (not present) in orange (blue). The heterodyne magnitude signal was not recorded for times t_s between 30 ms and 170 ms. Middle panel: Corresponding VCO frequency f . Bottom panel: Current in our atomic chip wires (red). Evaporation was induced by ramping up the current, which lowers the trap depth dynamically (see Fig. 6), and halted at 320 ms by ramping the current back down quickly. During evaporation (indicated by gray shading in all panels), the heterodyne magnitude was kept constant by a side-of-fringe lock. The atom-induced cavity shift was extracted from an in-loop measurement of the control voltage fed back to the VCO. At the end of an experimental run, a swept atom number measurement was performed, where δ_{pc} was varied by sweeping f down and up across cavity resonance. In these sweep measurements, the atom number was extracted from the shift of the cavity profile visible in the heterodyne magnitude signal, and was used just for calibration purposes.

probe-cavity detuning fixed at $\delta_{pc}/2\pi \approx \kappa/2\pi = 1.8\ \text{MHz}$ and thus the intracavity probe intensity constant. The time-zero of our measurement was chosen 8 ms after activating the feedback, which was enough time to avoid any effect of transients on our real-time traces. To realize the side-of-fringe feedback loop, part of the heterodyne signal was split off after a radio-frequency amplifier, sent through a bandpass filter with a $2\ \text{MHz}$ bandwidth, and its power was detected with a linear radio-frequency power detector (Analog Devices, AD8361). The detected power was kept constant by feeding back to the frequency of probe and LO through a voltage controlled oscillator (VCO) driving an acousto optic modulator (AO) before the cavity. The required in-loop control voltage was monitored. An equivalent VCO signal was recorded after the sequence without the atoms. The difference of this reference signal and the signal with atoms, together with the calibrated VCO characteristics, yielded the atom-induced cavity shift Δ_N . In order to reduce the effect of photon shot noise, we subtracted a running average of five empty cavity traces of successive runs from each trace with atoms. The number of averaged empty cavity traces was a compromise between mitigating the influence of shot noise on the reference trace and avoiding

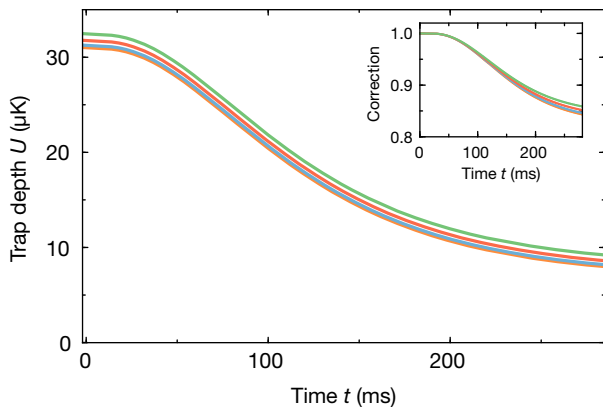


Figure 6. **Potential depth during forced evaporation.** The trap depth of the combined potential of far off-resonant optical lattice trap, magnetic field and probe-induced potential as the magnetic gradient is ramped up from zero to its maximal value. The inset shows the correction factor required to correct g^2 for the shift of the cloud relative to the maximal probe intensity. Different colors correspond to different intracavity photon number, with the color code the same as in Fig. 2.

additional imprecision due to longer-time technical drifts of the empty cavity resonance. After untilting the trap, we performed a swept atom number measurement, see Fig. 5. To this end, we swept the frequency of the cavity probe across the resonance of our cavity. The peak position of the recorded heterodyne signal relative to a reference measurement on an empty cavity taken at the end of the sequence reflected the atom-induced cavity shift, see Fig. 5. The swept measurement was used to benchmark the shift correction described in the next section.

Trap depth and shift correction

The magnetic field applied during evaporative cooling leads to a reduction of the trap depth to below $10 \mu\text{K}$, see Fig. 6. We find the trap depth using the known waist size of the lattice trap in the cavity and the applied magnetic fields as the height of the saddle point of the combined potential of magnetic and optical traps relative to the trap bottom, including the small but non-negligible influence of the red-detuned probe. With increasing applied magnetic field gradients, the trap minimum is radially displaced from the center of the cavity mode, and hence away from the maximal coupling point of the probe laser. We calculate the displacement and the resulting reduced overlap with the probe laser for a point-like cloud. The maximal displacement is approximately $8 \mu\text{m}$. For our probe waist of $w_p = 25 \mu\text{m}$, this displacement leads to a change in g^2 and hence Δ_1 of at most 15% (see the inset of Fig. 6). We verified that the results of this procedure for a point-like cloud were almost identical to the case of a thermal cloud with a temperature of $T_0 \approx 2.6 \mu\text{K}$, such that we use the former

as an approximation for the latter. We confirm the accuracy of our calculated correction factor by comparing the corrected atom number measured at the maximal spatial displacement with a sweep measurement after removing the magnetic field gradient, see Fig. 5, where the atoms were located at the position of maximal probe coupling. Due to the strong lattice-induced confinement, the displacement of the cloud along the vertical direction is negligible. In addition to the sideways displacement, the applied magnetic field rotates the overall magnetic field direction. Consequently, the orientation of the quantization axis tilts and the projection of the circularly polarized light of the probe beam changes, resulting in maximally 3% of additional correction to the coupling strength. We stress that the small correction of g^2 does not affect any of the conclusions drawn, and we have accounted for it in the direct quantitative comparison of our measurements with the theoretical models presented in the following.

APPENDIX B: MODELING EVAPORATIVE COOLING

Theoretical model for evaporation

We model evaporative cooling in two dimensions, following references [25, 28], by the time evolution of a truncated Maxwell-Boltzmann distribution in a trap with time-dependent depth. The change in atom number N for a truncation parameter $\eta = U/k_B T$ in the trap is

$$\dot{N} = -N\gamma e^{-\eta} \left(\frac{\eta P(2, \eta) - 3P(3, \eta)}{P(2, \eta)^2} \right). \quad (2)$$

Here, $\gamma = n_{th}\sigma v_{th}$ is related to the elastic collision rate $\gamma_c = \sqrt{2}\gamma$ in a gas with density n_{th} and thermal velocity $v_{th} = \sqrt{8k_B T/\pi m}$. The incomplete Gamma functions $P(\alpha, \eta) = \int_0^\eta dt t^{\alpha-1} e^{-t}/\Gamma(\alpha)$ take into account truncation effects in a trap with finite depth [25]. We can rewrite Eq. (3) to bring out the temperature and atom number dependence explicitly,

$$\dot{N} = -c_\gamma N^2 T^{-\frac{1}{2}} e^{-\eta} \left(\frac{\eta P(2, \eta) - 3P(3, \eta)}{P(2, \eta)^2} \right). \quad (3)$$

The constant $c_\gamma = \gamma_0 T_0^{\frac{1}{2}}/N_0$ contains the initial rate γ_0 , the initial temperature T_0 and the initial atom number N_0 . Notably, Eq. (3) indicates that, at constant temperature, atom spilling over a potential barrier constitutes a loss process which is non-linear in atom number. Evaporating atoms cause a change in the internal energy $E = 2Nk_B T$ of the gas. Taking the time derivative and solving for the change in temperature, we obtain

$$k_B \dot{T} = \frac{\dot{E}}{2N} - \frac{\dot{N}}{N} k_B T. \quad (4)$$

The change in energy is proportional to the atom loss rate multiplied with the energy of a leaving atom, corrected

for truncation [25]

$$\dot{E} = \dot{N} k_B T \left[\eta + \left(1 - \frac{P(4, \eta)}{\eta P(2, \eta) - 3P(3, \eta)} \right) \right], \quad (5)$$

where $\eta = U/k_B T$. Plugging this into Eq. (4), we obtain the change in temperature as

$$\frac{\dot{T}}{T} = \frac{1}{2} \frac{\dot{N}}{N} \left[\eta - \left(1 + \frac{P(4, \eta)}{\eta P(2, \eta) - 3P(3, \eta)} \right) \right] + \frac{\Gamma_h}{2T}. \quad (6)$$

In the last step, we have included a heating rate Γ_h , caused, e.g., by photon recoil heating or other external heating sources.

Three-body losses affect both the atom number dynamics and the temperature dynamics of evaporative cooling. Their atom number dynamics have to be treated separately from the atom number dynamics due to evaporating atoms. The atom loss rate due to three-body collisions is

$$\dot{N}_{3B} = -c_3 \frac{6}{\sqrt{27}} L_3 n_{th}^2 N \propto \frac{N^3}{T^2}. \quad (7)$$

Here, L_3 denotes the three-body loss coefficient [39], which is scaled appropriately for a thermal bosonic gas [40], and c_3 is an additional scaling coefficient. These losses do not contribute to the cooling of the gas. Rather, they lead to “anti-evaporation heating” [40], as the loss happens predominantly at the center of the trap, where the density is highest. Atoms in the central region of the trap have less than average potential energy, such that the gas effectively heats upon thermalization. Quantitatively, anti-evaporation heating leads to a change in temperature reflecting the difference in potential energy between an average atom and an atom lost through a three-body collision,

$$\left(\frac{\dot{T}}{T} \right)_{3B} = -\frac{1}{2} \frac{\dot{N}_{3B}}{N} \left(1 - \sqrt{\frac{2}{3}} \right) \quad (8)$$

Together with the known time-dependent trajectory of the trap depth $U(t)$, equations (3) and (6) can be solved to obtain the mean atom number and temperature dynamics of evaporative cooling. The effect of three-body loss can be included by adding equations (7) to (3) and (8) to (6).

Evaporation dynamics

The model derived in the previous section can be used to check the influence of initial atom number and temperature variations on the evaporation dynamics, and serves as a benchmark of the subtracted slope presented in the main text as a measure of non-linear dynamics in the average evolution. To this end, we simulate the coupled atom- and temperature dynamics for our experimental configuration. We neglect the influence of adiabatic decompression [28], which is expected to be small in

gradient-assisted evaporation [41]. In our case, the expected reduction of the trap frequency along the direction of the gradient is approximately 15%. The heating rate per photon is extracted from reference measurements to be $\Gamma_h = 7(3) \mu\text{K s}^{-1}$. For our parameters, we expect scattering into free space to be a significant heating source. The off-resonant scattering rate $\Gamma_{\text{eff}}/n \approx 3.6 \text{ s}^{-1}$ leads to an expected recoil heating rate per intracavity photon of $\Gamma_r/n = 2E_r \Gamma_{\text{eff}}/n \approx h \times 27.1 \text{ kHz s}^{-1} = k_B \times 1.3 \mu\text{K s}^{-1}$, where we have used the recoil energy $E_r = \hbar^2 k^2 / 2m \approx h \times 3.8 \text{ kHz}$ for ^{87}Rb on the $D2$ line. We attribute the discrepancy between this estimate and the experimental value to additional technical noise contributions from the side-of-fringe lock, which can lead to parametric heating of the cloud.

To model fluctuations in the initially prepared ensemble, we calculate 200 traces with atom number N_0 and temperature T_0 drawn from Gaussian distributions. The standard deviation of the atom number distribution is extracted from a fit to the measured initial atom number distribution. The standard deviation of the temperature distribution ΔT_0 is varied in the simulation. The elastic collision rate is calculated for each run using the drawn atom number and temperature assuming a quasi two-dimensional gas. The resulting curves of the time evolution of the atom number for our trap ramp are shown in Fig. 7a, for a temperature spread of $\Delta T_0 = 0.6 \mu\text{K}$ and a three-body collision scale factor $c_3 = 0.2$. The overall temporal dynamics and the final atom numbers are in good agreement with the data for the chosen parameters. During the initial 100 ms of the evaporation process, the temperature fluctuations, reflected in fluctuations in the ratio of trap depth to temperature η , are rapidly suppressed and temperature locks to an approximately fixed fraction of trap depth provided the heating is small, see Fig. 7b.

In order to support the introduction of the subtracted slope $a_s = \rho_{12} \sigma_2 / \sigma_1 - p$ as a non-linearity measure (see main text and Appendix C), we study the effect of varying temperature spread and three-body loss on a_s . The resulting dependencies are shown in Fig. 7c and Fig. 7d. We observe that, as expected and explained in the main text, an increase in the initial temperature spread is reflected as a positive signal in a_s , which reduces to near zero and stays constant for later initial time t_1 . Contrarily, the introduction of strong three-body loss in the dynamics results in a negative a_s and hence sublinear behavior, as expected for an effect that reduces the atom number variance in time [29], even if strong initial temperature fluctuations are present in the ensemble, see Fig. 7d. Qualitatively, the simulation shows the same features as observed in our data for three-body losses of approximately $c_3 = 0.05 - 0.2$ times the value expected according to Eq. (7). This reduction of three-body losses points to an overestimate of the density of the ensemble, for example due to interactions in the two-dimensional gas, which we have neglected in our treatment. Our simulations support our claim that the subtracted slope a_s

is a meaningful quantity sensitive to both initial temperature fluctuations and three-body loss. We have verified that this is robustly the case also if the thermalization and heating rates are reduced. For stronger heating, we find experimentally and from our simulations that evaporation assumes linear character with $a_s = 0$. While our simulations do reflect the effect of fluctuations in the initial ensemble, we stress that the intrinsic stochastic character of evaporation is not captured. Further studies of the interplay between stochastic fluctuations and non-linearities such as three-body loss would be of particular interest.

APPENDIX C: EVAPORATION NON-LINEARITY AND NOISE

Non-linearity measure

The minimally invasive measurement strategy involving the cavity allows to go beyond single-time observables by constructing two-time correlations. The information about the linearity of the time evolution is encoded in the dependence of the measured atom number N_2 on the initial atom number N_1 . Here, we denote N_1 and N_2 as ensembles of measured atom number outcomes at times t_1 and t_2 respectively. The standard deviations of the distributions are denoted σ_1 and σ_2 respectively. Assuming a linear relationship between N_1 and N_2 , the optimal set of coefficients a and b of the model $f(X, \beta) = aX + b$ can be found from linear regression analysis for the variables N_1 and N_2 . The parameters minimizing the squared residuals are

$$a = \rho_{12} \frac{\sigma_2}{\sigma_1} \quad (9)$$

$$b = \langle N_2 \rangle - a \langle N_1 \rangle. \quad (10)$$

Here, we have introduced the Pearson correlation coefficient

$$\rho_{12} = \frac{\text{cov}(N_1, N_2)}{\sigma_1 \sigma_2} \quad (11)$$

calculated from the covariance of the two random variables. When standardizing the random variables by subtracting their mean and normalizing to the standard deviation, $N_{1(2),s} = (N_{1(2)} - \langle N_{1(2)} \rangle) / \sigma_{1(2)}$, the correlation coefficient corresponds directly to the slope of the straight line minimizing the ordinary least squares in the scatter plot. A decreasing correlation coefficient in this case directly reflects the influence of measurement and stochastic noise in the system. Scatter plots of $N_{2,s}$ vs. $N_{1,s}$ are shown in Fig. 2 in the main text. To extract the non-linearity measure, we consider non-standardized variables. Here, for a strictly linear relationship, the fraction of remaining atoms $p = \langle N_2 \rangle / \langle N_1 \rangle$ contains the full information on the dynamics. Therefore, it should hold that $a = p$ in this case. Any deviation from $a = p$ can

be interpreted as a non-linearity and leads to increased ($a > p$) or decreased ($a < p$) relative fluctuations in the ensemble at time t_2 . On average, $a < p$ ($a > p$) implies a better (worse) predictive power of a measurement result obtained at time t_1 for a measurement performed at time t_2 . As an example, if the atom loss dynamics has a character $\dot{N} \propto -N^\alpha$, $\alpha > 1$, we expect realizations with more atoms initially to lose atoms more quickly. This leads to a value of $a < p$ for later times, as more atoms were lost than expected for a linear process. Therefore, a loss process with $\alpha > 1$ reduces atom number fluctuations in an ensemble, which has been observed experimentally for a cloud with three-body loss ($\alpha = 3$) [29] and is consistent with the simulations shown in Fig. 7d.

Unexplained variance

The correlation coefficient quantifies the degree of fluctuation between two random variables which can be explained by a linear model. For stochastic processes such as evaporative cooling or other transport phenomena, the fluctuations due to this randomness are also of interest. Relating measurements of an atom number N_2 at time t_2 to measurements N_1 at time t_1 of the same ensemble can shed light on this process noise, as it appears as fluctuations in N_2 which are not explained by any correlation with N_1 .

We can quantify this ‘‘unexplained variance’’ by evaluating

$$\sigma_u^2 = \sigma_2^2 (1 - \rho_{12}^2). \quad (12)$$

Here, the correlation coefficient captures the fraction of the total variance explained by the linear relationship, which is subtracted from the total variance to obtain the unexplained variance. We evaluate the fraction of unexplained variance for our data, see Fig. 4.

Unexplained variance for uncorrelated atom loss

In the following, we will derive an expression for σ_u assuming a given constant measurement noise σ_m and a purely Poissonian ejection mechanism of atoms with corresponding stochastic noise. Under these assumptions, we expect the variance $\sigma_{2,th}$ at time t_2 to contain contributions from measurement noise, stochastic noise and fluctuations σ_1 of N_1 . Concretely, we get

$$\sigma_{2,th}^2 = p^2 (\sigma_1^2 - \sigma_m^2) + \sigma_m^2 + \langle N_1 \rangle p(1 - p). \quad (13)$$

The second and third term are measurement noise and Poissonian stochastic noise, respectively. The first term reflects the scaled initial ensemble fluctuations, which are obtained from the part of the fluctuations σ_1 which is not originating from measurement noise. The prediction for

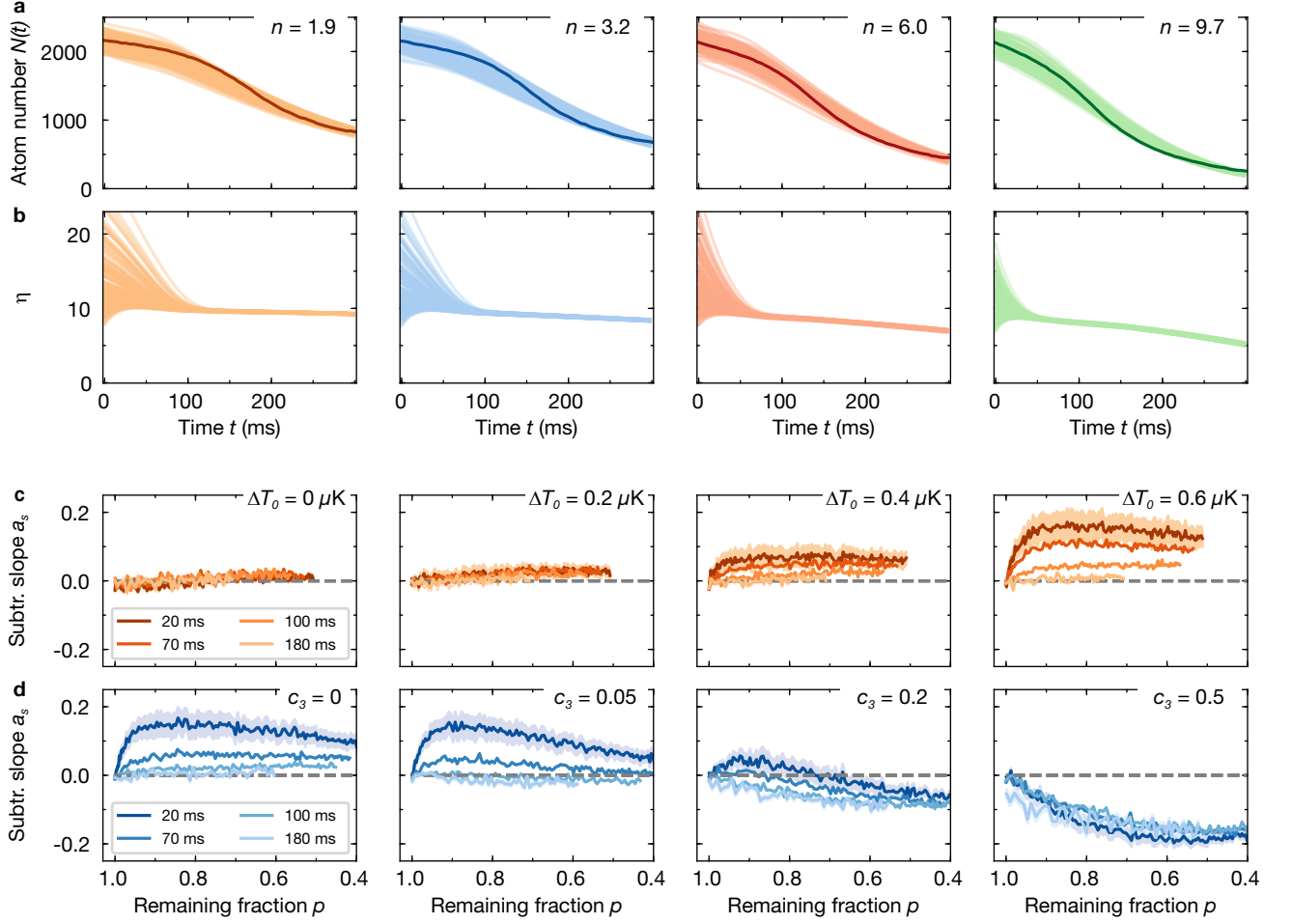


Figure 7. **Theoretical modeling of evaporation.** **a** Simulation of atom number dynamics during forced evaporation for the trap ramp shown in Fig. 6. We show 200 traces with initial atom numbers N_0 and temperatures T_0 sampled from Gaussian distributions in light color, for varying intracavity photon number n as indicated in the top right corner. The atom number samples have a mean $\langle N_0 \rangle$ and a standard deviation of $2\langle N_0 \rangle^{1/2}$. The temperature distribution is centered about the initial temperature T_0 and has a standard deviation of $\Delta T_0 = 0.6 \mu\text{K}$. We have included a three-body loss contribution scaled by $c_3 = 0.2$. The dark line shows the measured atom number dynamics including shift correction. **b** Ratio of trap depth to temperature, $\eta = U/k_B T$, for the same ensemble as in **a**. The initially broad distribution is rapidly narrowed down and then remains nearly constant during further evaporation. **c** Subtracted slope a_s for $n = 1.9$ for different temperature spreads (indicated in top right corner) in absence of three-body loss ($c_3 = 0$). We observe the same trends as observed in our experiment, with a fast rise for small p and a decay with increasing initial time t_1 (indicated in legend). The shaded region indicates the standard deviation extracted from a bootstrap analysis of the calculated samples. **d** Subtracted slope a_s for $n = 3.2$ and $\Delta T_0 = 0.6 \mu\text{K}$ for increasing contribution of three-body loss characterized by the scaling factor c_3 (indicated in top right corner). Three-body loss leads to a negative contribution to a_s , which suppresses the effect of initial temperature variations.

the correlation coefficient defined in Eq. (11) becomes

$$\rho_{12,th} = \frac{p(\sigma_1^2 - \sigma_m^2)}{\sqrt{\sigma_{2,th}\sigma_1}}. \quad (14)$$

In the covariance in the numerator, only those parts of the variances without the measurement noise contribute. Note that this is strictly true only outside the correlation time of the measurement noise, which we assume to be white for simplicity. For equal-time measurements, the correlation coefficient equals unity. Using Eq. (13)

and Eq. (14), we can get a prediction for the fraction of variance unexplained,

$$\sigma_{u,th}^2 = \sigma_{2,th}^2 (1 - \rho_{12,th}^2) \quad (15)$$

$$= p^2 \frac{\sigma_m^2}{\sigma_1^2} (\sigma_1^2 - \sigma_m^2) + \sigma_m^2 + \langle N_1 \rangle p(1-p). \quad (16)$$

This expression shows that the unexplained variance is affected by the initial variance, measurement noise and stochastic noise. Comparing with the expression for the

variance $\sigma_{2,th}^2$, we see that the contribution from the initial variance is suppressed for small measurement noise $\sigma_m^2 \ll \sigma_1^2$. We compare this model to our data in Fig. 4. The measurement noise σ_m is extracted from the Allan deviation shown in Fig. 1e and the initial mean $\langle N_1 \rangle$ and standard deviation σ_1 are evaluated from the atom number distribution at time t_1 . The most striking discrepancy is caused by temperature fluctuations: Initially hidden, they are converted to strong atom number fluctuations upon cutting into the thermal distribution. These fluctuations are not expected based on earlier atom number measurements alone. At later times, the unexplained variance approaches the prediction for uncorrelated atom loss. The good agreement between this simple model and our data at late times indicates that technical noise has a negligible impact on our measurements. The convex shape proportional to $p(1-p)$ of fraction of variance unexplained is masked to a large part by the first term in $\sigma_{u,th}$, despite the small imprecision reached by cavity-assisted atom number detection.

APPENDIX D: MEASUREMENT PRECISION

In the following, we show that the enhanced atom light-coupling in an optical cavity is fundamental to high-precision atom counting. Minimally invasive measurements compromise between excess heating and consecutive fluctuations due to the measurement process and a sufficient number of extracted photons to reduce photonic shot noise [37, 42, 43]. For cavity-aided atom counting, we aim to find an optimal observation time as a compromise between averaging down photon shot noise of the detected probe field and probe-induced atom number fluctuations, e.g. by recoil heating or cavity backaction heating [12–15]. To quantify the photonic shot noise contribution, we use the Lorentzian cavity profile for the photon number n in the cavity

$$n = n_{\max} \frac{\kappa^2}{\kappa^2 + \delta_{pc}^2}. \quad (17)$$

Here, n_{\max} denotes the on-resonance ($\delta_{pc} = 0$) intracavity photon number and κ is the half linewidth of the cavity. The sensitivity $\Delta\delta_{pc}$ for determining the cavity-probe detuning as a function of photon noise Δn is obtained by taking the derivative of Eq. (17) with respect to δ_{pc} ,

$$\frac{\Delta n}{n} = -2 \frac{\delta_{pc}^2}{\kappa^2 + \delta_{pc}^2} \frac{\Delta\delta_{pc}}{\delta_{pc}}. \quad (18)$$

At the side of fringe $\delta_{pc} = \kappa$, the sensitivity becomes $\frac{\Delta n}{n} = -\frac{\Delta\delta_{pc}}{\kappa}$. Taking into account the detection efficiency ϵ of the detection chain, the number of detected photons within a window of integration time τ is $n_{\det} = 2\kappa n \epsilon \tau$. Note that for a heterodyne detector, the detection efficiency effectively reduces by a factor 2 ($\epsilon \rightarrow \epsilon/2$) if only the magnitude of the heterodyne signal is used in the detection, as is the case in our, in this

sense, non-optimal feedback scheme. Assuming photon-shot noise $\Delta n_{\det} = \sqrt{n_{\det}}$, we find the uncertainty

$$\Delta\delta_{pc} = -\sqrt{\frac{\kappa}{2n\epsilon\tau}}. \quad (19)$$

Using the cavity shift per atom, Δ_1 , we convert this to an atom number uncertainty

$$\Delta N = \frac{\Delta_{ca}}{g^2} |\Delta\delta_{pc}| = \frac{\Delta_{ca}}{g^2} \sqrt{\frac{\kappa}{2n\epsilon\tau}} = \sqrt{\frac{1}{2C}} \sqrt{\frac{1}{\Gamma_{\text{eff}}}} \sqrt{\frac{1}{\epsilon\tau}}. \quad (20)$$

In the last step, we have introduced the cooperativity $C = g^2/\kappa\Gamma$ for a vacuum Rabi coupling $g = \sqrt{d^2\omega_a/2\hbar\epsilon_0 V_m}$ on the optical transition with frequency ω_a and dipole matrix element d and for a cavity mode volume V_m . The dependence of the uncertainty on the cooperativity shows the advantage of a cavity-assisted measurement over its free-space equivalent. Furthermore, the fluctuations due to photonic shot noise decrease with the number of scattered photons $\Gamma_{\text{eff}}\tau$. The total number of scattered photons is also responsible for heating the cloud via recoil heating with a rate Γ_r , which introduces atom number loss and associated fluctuations in a trap with finite depth. Assuming Poissonian fluctuations in the number of lost atoms within an integration time τ , we model the fluctuations in atom number in a trap with depth U as

$$\Delta N^2 = N \frac{\alpha\Gamma_r}{U} \tau = N \Gamma_{\text{eff}} \frac{\alpha E_r}{U} \tau. \quad (21)$$

The proportionality constant α allows to take into account truncation in evaporative cooling. We can add the fluctuations due to atom loss to the photonic shot-noise-induced fluctuations derived in Eq. (20) and obtain

$$\Delta N_{\text{tot}}^2 = \frac{1}{2C} \frac{1}{\Gamma_{\text{eff}}} \frac{1}{\epsilon\tau} + N \Gamma_{\text{eff}} \frac{\alpha E_r}{U} \tau. \quad (22)$$

Minimizing the uncertainty with respect to τ , we get

$$\Delta N_{\text{tot,min}}^2 = N \sqrt{\frac{2}{NC\epsilon}} \sqrt{\frac{\alpha E_r}{U}} \quad (23)$$

at a corresponding integration time

$$\tau_{\text{min}} = \frac{1}{\Gamma_{\text{eff}}} \sqrt{\frac{1}{2NC\epsilon}} \sqrt{\frac{U}{E_r\alpha}}. \quad (24)$$

We want to minimize both the minimal fluctuations as well as the corresponding integration time. Short integration times correspond to maximal dynamic range for measuring atom number dynamics. We see that both quantities benefit from a cavity with high cooperativity. Also, the dependence on collective cooperativity NC shows that precise cavity-aided atom counting is easier to achieve at larger atom numbers. Interestingly, the minimal atom number imprecision does not depend on

the effective scattering rate Γ_{eff} . We observe that the minimal atom number imprecision has no fundamental limit, as the ratio E_r/U can be reduced by increasing the trap depth, which reduces the loss. If temperature is a relevant parameter in the probed dynamics, a further interesting quantity to take into account is the temperature increase of the gas during the integration time. From the increase in internal energy and assuming equipartition in a two-dimensional harmonically trapped gas, it is given as

$$k_B \Delta T_{\text{min}} = \frac{2\Gamma_{\text{eff}} E_r \tau_{\text{min}}}{2} \quad (25)$$

$$= \sqrt{\frac{1}{2NC\epsilon}} \sqrt{\frac{UE_r}{\alpha}}. \quad (26)$$

Taking the product of temperature added and minimal atom number uncertainty, the experiment-specific quantities U and α drop out and we are left with

$$\left(\frac{k_B \Delta T_{\text{min}}}{E_r} \right) \left(\frac{\Delta N_{\text{tot, min}}^2}{N} \right) = \frac{1}{NC\epsilon}. \quad (27)$$

This relation implies that for a given minimal integration time, the energy deposited in the system bounds the atom number imprecision and vice versa. The exact value for the minimal integration time and thus the time resolution of the measurement can be chosen by changing the effective scattering rate, i.e. the atom-cavity detuning Δ_{ca} in our case. Our observed dependence of the imprecision quantified by the Allan deviation with integration time τ is shown in Fig. 1e, where we find a decrease of the imprecision with increasing integration time for small $\tau < 1$ ms and then an increase for larger τ . We note, however, that there the increase in imprecision is dominated by the dynamically changing mean atom number, which leads to a scaling of the Allan variance with τ^2 . Directly comparing the two cases requires subtracting the known time dynamics of the mean atom number, only keeping the stochastic contribution ($\propto \tau$) discussed here. While these two effects can always be separated in post-processing even for an unknown dynamical process by subtracting the mean of all traces, this is generally not possible e.g. for applying feedback to a system with unknown atom number dynamics.